High-Q metasurface biosensor based on low-refractive-index materials

GEFEI ZHAO[1,2], XIAOLI ZHANG[3], YINGXIAN WANG[3], JIESHUANG QI[4], YING TIAN[4], XIAOMEI ZHANG[5], ZHIBO YIN[6,*], YONGXING JIN[4,*]

[1]*Institute of Medical Technology, Peking University Health Science Center, Beijing, 100191, China*
[2]*Biomedical Engineering Department, Institute of Advanced Clinical Medicine, Peking University, Beijing, 100191, China*
[3]*Special Equipment Institute, Hangzhou Polytechnic University, Hangzhou 310018, People's Republic of China*
[4]*Institute of Optoelectronic Technology, China Jiliang University, Hangzhou 310018, China*
[5]*Hangzhou QiuShi New Materials Technology Co., Ltd., Hangzhou, China*
[6]*School of artifical intelligence, Zhejiang Polytechnic University of Mechanical and Electrical Engineering, Hangzhou, Zhejiang, 310051, China*

This study presents a metasurface biosensor constructed from low-refractive-index materials that successfully achieves high-Q unit structures through the synergistic optimization of material selection and geometric parameter design. Simulation verification was conducted using photopolymer resin and aluminum oxide as comparative materials. The results indicate that photopolymer resin, due to its low refractive index, significantly reduces light scattering loss and demonstrates exceptional overall performance in theoretical simulations, achieving a Q-factor of 737.6 and a refractive index sensing sensitivity of 51.31 GHz/RIU. More importantly, the photopolymer-based metasurface retains high Q-factor characteristics while exhibiting enhanced biomolecular adsorption capabilities. This research offers an innovative solution for developing high-performance and cost-effective biosensing platforms.

(Received October 13, 2025; accepted June 2, 2026)

Keywords: Metasurface, Biosensor, Terahertz

1. Introduction

Terahertz waves are electromagnetic waves with frequencies ranging from 0.1 to 10 THz, corresponding to wavelengths between 3 mm and 30 μm. These waves occupy a position between microwave and infrared waves in the electromagnetic spectrum [1-4]. This frequency band lies in the transition region between electronics and photonics and is commonly referred to as the terahertz gap. The unique properties of terahertz waves provide significant advantages for biological detection applications.

In recent years, metasurface bio-devices have demonstrated considerable promise as innovative tools for optical biosensing and have been applied across various biomedical fields, including fluorescence imaging [5,6], endoscopic optical coherence tomography [7], and the sensing and detection of biomolecules such as proteins [8,9], deoxyribonucleic acid (DNA) [10,11], cancer markers [12,13], and cells [14]. Biosensors utilizing metasurfaces offer several advantages over traditional biological devices, including user-friendliness, portability, elimination of labeling requirements, and self-referencing capabilities [15,16], providing a highly sensitive platform for cell detection. Conventional optical biosensing and imaging equipment is often large and cumbersome, significantly limiting its clinical applicability [17,18]. In contrast, metasurface biosensors typically feature compact designs, enabling their use in diverse environments such as hospitals, residences, and outdoor locations. Due to their subwavelength structures, metasurface sensors exhibit exceptional sensitivity to specific substances, allowing the detection of biomolecules even at extremely low concentrations [19-23].

Since the introduction of metasurface biosensors, scientists have continuously improved their performance to enhance detection capabilities by exploring various materials and designs. Current research focuses on all-dielectric metasurface biosensors [24-27], plasmonic metasurface biosensors [28-31], and hybrid metasurface biosensors [32-36]. The corresponding statement has been refined to: in recent years, terahertz metasurface sensors have demonstrated significant application potential in biomolecular detection, refractive index sensing, and chiral recognition [37-38]. However, devices based on high-refractive-index materials currently suffer from substantial scattering losses. The use of low-refractive-index materials is particularly important. These materials effectively minimize light scattering and reflection, enhancing the interaction between light and the target substance, thereby improving the performance of metasurface biosensors. Furthermore, many low-refractive-index materials exhibit high biocompatibility, which reduces interference and

damage to biological samples, broadening their potential applications in biosensing. Among these materials, photopolymer resin is especially noteworthy. It not only possesses a low refractive index but also simplifies the fabrication process of metasurfaces, significantly enhancing sensor performance. Consequently, incorporating photopolymer resin into metasurface biosensors offers valuable insights and technical support for advancing high-performance biosensors.

In this study, we develop a metasurface biosensor utilizing low-refractive-index materials, specifically photopolymer resin and aluminum oxide, and perform structural design and optimization. Our analysis of the simulation results indicates that breaking the symmetry of the metasurface structure leads to a high-quality factor (Q-factor). A comparison of the two materials reveals that the resin offers significant advantages for biosensor applications. The resin-based metasurface biosensor exhibits a sharp resonance peak within the 0.73 – 0.74 THz frequency range, achieving a theoretical sensitivity of 51.31 GHz/RIU and a theoretical Q-factor of 737.6, demonstrating exceptional sensing capabilities. This design provides new perspectives and methodologies for developing high-sensitivity terahertz biosensors.

2. Design and results

Fig. 1 (a) presents the schematic diagram of the metasurface structure we developed, while Fig. 1(b) illustrates the schematic of the unit cell structure. The photopolymer resin used has a dielectric constant of 2.89. The metasurface structure consists of a substrate with a thickness of H = 500 μm and a structural layer thickness of T = 200 μm,with unit structure dimensions of P1 = 300 μm and P2 = 400 μm. The unit structure of the metasurface comprises two elliptical cylindrical shapes that are symmetric along the y-axis. Each elliptical cylinder is rotated inward at an angle θ of 10°, breaking the rotational symmetry. The short axis of each elliptical structure measures R1 = 75 μm, while the long axis measures R2 = 100 μm. These unit structures are periodically arranged to form a metasurface biosensor. To evaluate the performance of the metasurface, we employed the time-domain finite integral method, applying periodic boundary conditions in the x and y directions and an open boundary condition in the z direction. The electric field is oriented along the y-axis,with terahertz waves incident perpendicularly on the metasurface. We computed the transmission curves within the 0.66–0.76 THz range, as shown in Fig. 1(c), where a distinct transmission peak is observed at 0.7376 THz.

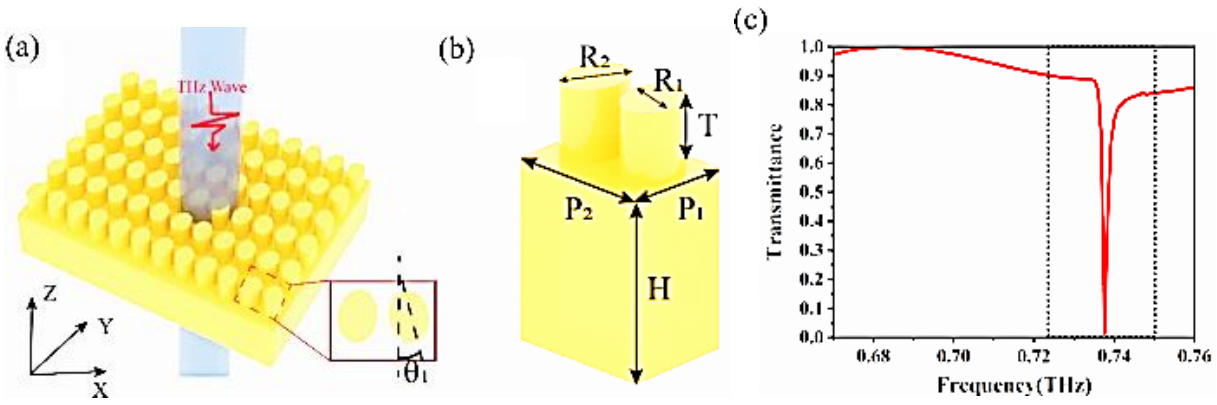

Fig. 1. (a) Diagram illustrating the structure of the metasurface; (b) Diagram depicting the unit cell of the metasurface; (c) Graph showing the transmittance curve (colour online)

We calculated and visualized the distribution of electric and magnetic field energy for the metasurface at a frequency of 0.7376 THz, as shown in Fig. 2 (a) and Fig. 2 (b) display the electric field energy distributions in the x-y and x-z planes, respectively. These figures indicate that at the resonance peak, the electric field is predominantly concentrated at the base of the elliptical nanocolumns and on the substrate adjacent to the elliptical structures. This localized enhancement of the electric field enhances the interaction between biomolecules and the surface, thereby increasing the sensitivity and response efficiency of the metasurface in biosensing applications. Fig. 2 c) and Fig. 2 (d) illustrate the magnetic field energy distributions in the x-y and x-z planes at 0.7376 THz, respectively. These figures demonstrate that the magnetic field of the metasurface is primarily concentrated at the bottom of the elliptical nanocolumns and on the substrate between the elliptical structures. The distribution of the magnetic field differs from that of the electric field, and the areas of concentration for both fields are closely related to the geometric shape of the elliptical columns.

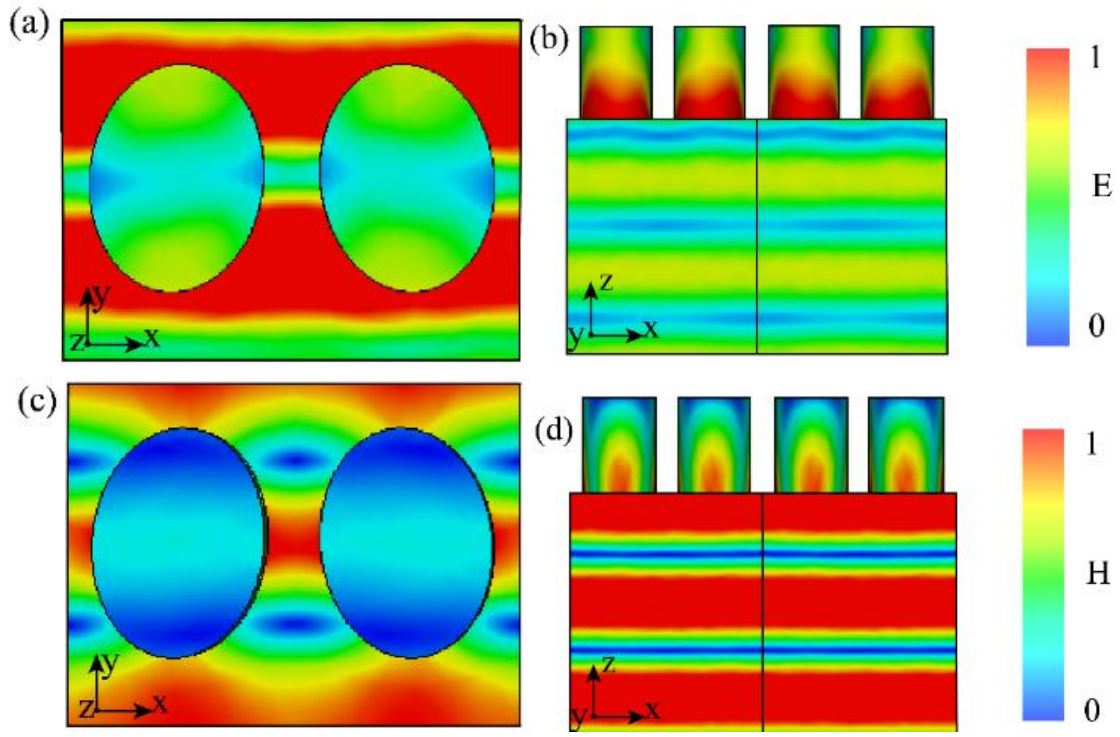

Fig. 2. The near-field energy distribution of the metasurface. (a) Diagram illustrating the electric field energy distribution in the x-y plane. (b) Diagram depicting the electric field energy distribution in the x-z plane. (c) Diagram showing the magnetic field energy distribution in the x-y plane. (d) Diagram representing the magnetic field energy distribution in the x-z plane (colour online)

The alteration in the rotation angle of the two elliptical nanorods disrupts the structural symmetry. This symmetry breaking motivated a systematic analysis of how varying rotation angles θ affect the resonant properties of the metasurface. Specifically, we examined the transmission spectral characteristics of the metasurface for vertically incident terahertz waves as θ was varied from 0° to 10° in 2° increments, as illustrated in Fig. *3*(a) the simulation results indicate that the position of the resonance peak remains relatively stable despite changes in θ. We also calculated the Q-factor and full width at half maximum (FWHM) values of the metasurface in relation to the rotation angle θ, as depicted in Fig. 3 (c) notably, the FWHM exhibits significant variation: as θ increases from 0°, it initially decreases rapidly, reaching a minimum of 7.8 GHz at θ = 6° , before rising again with further increases in θ. The Q-factor is determined using the formula Q = λ / FWHM. Analysis of the Q-factor variation with angle reveals that the peaks at 737.6 when θ = 6°, This dynamic control feature represents a 42% enhancement compared to the original symmetric structure. These results show that adjusting the structural symmetry of the nanostructure enables the dynamic modulation of the metasurface's resonance Q-factor. At θ = 6, the metasurface achieves high-Q resonance, exhibiting the most distinct resonance characteristics and optimal performance.

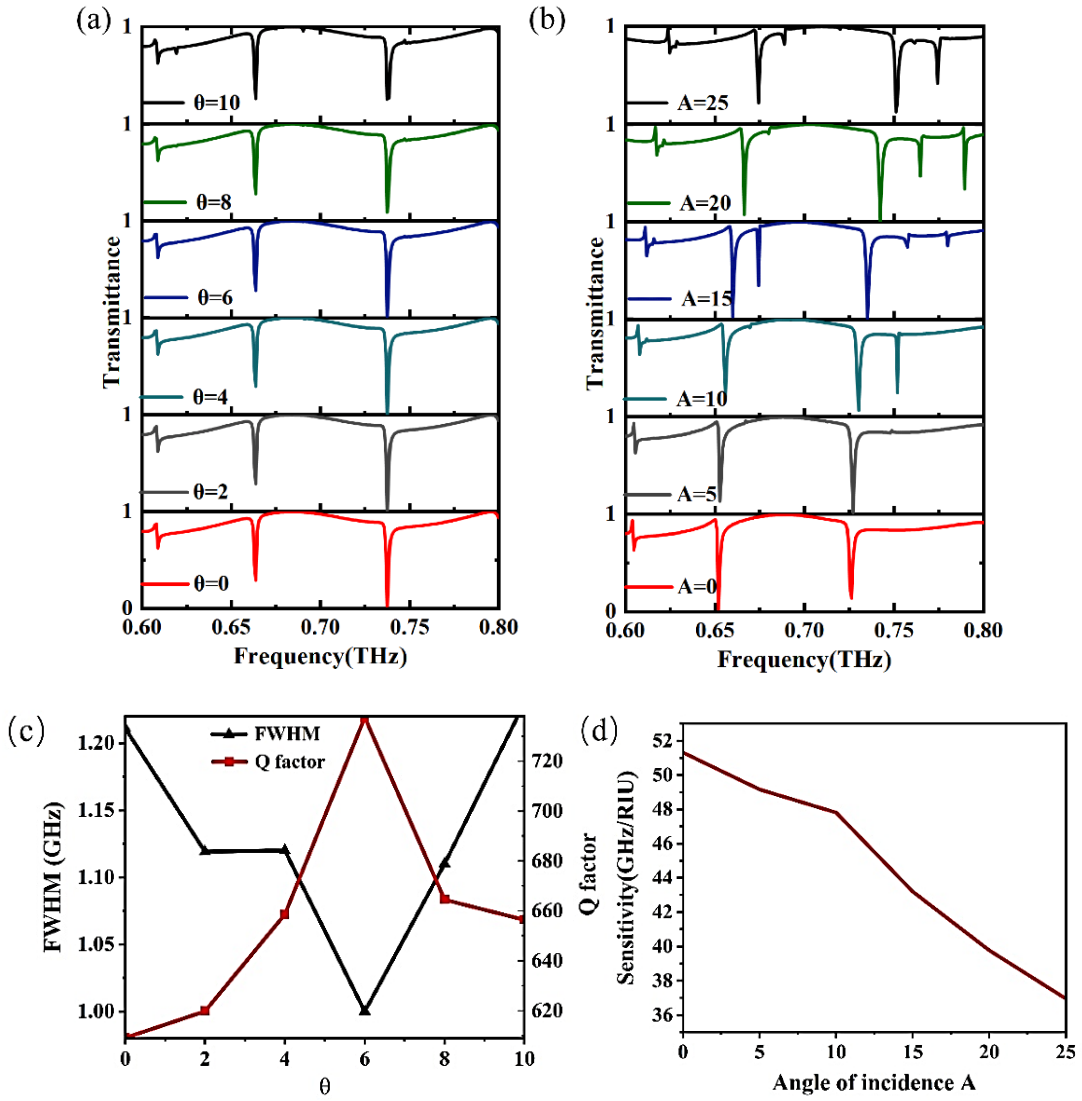

Fig. 3. (a) The transmission spectrum of the metasurface varies with the rotation angle θ; (b) The transmission spectrum of the metasurface changes based on the incident angle A; (c) The Q-factor and FWHM of the metasurface are plotted against the rotation angle θ; (d) The sensitivity of the metasurface is presented as a function of the incident angle A (colour online)

To investigate the effect of different incident angles of terahertz light on the performance of metasurfaces, we adjusted the angle of incidence, denoted by A. By varying A from 0° to 25° in 5° increments, we obtained the corresponding transmittance spectra shown in

Fig. 4(b). As illustrated, increasing A results in sharp resonance peaks within the 0.72–0.74 THz range, with the resonance peak positions exhibiting a noticeable blue shift. This indicates that changes in the incident angle significantly influence the resonance frequency. Additionally, the metasurface's response to analyte variations at different incident angles was simulated, as shown in

Fig. 4(d). It is evident that as A increases from 0° to 25°, the sensitivity of the metasurface gradually decreases. The highest sensitivity and optimal performance occur at an incident angle of 0°, when the incident light is perpendicular to the surface.

To evaluate the impact of structural parameters under real manufacturing conditions, we conducted a comprehensive examination of how substrate thickness H and structural layer height T affect the performance of the metasurface. Actual production requires a substrate thick enough to ensure structural stability and prevent deformation during both fabrication and usage. Fig. 5(a) illustrates the transmission spectrum of the metasurface's transmission peak in relation to substrate thickness H, which ranges from 300 μm to 600 μm. We observed that increasing the substrate thickness from 400 μm to 500 μm resulted in a redshift in transmission. In contrast, variations in structural height T had minimal impact on the resonance frequency, as shown in Fig. 5(b). When T was adjusted between 100 μm and 175 μm, the position of the resonance peak remained largely unchanged, indicating that the resonance frequency is not significantly affected by changes in height. Fig. 5(c) shows how the Q-factor of the

metasurface varies with substrate thickness H. Initially, as H increases, the Q-factor rises, then declines, peaking at H = 500 μm. Therefore, to achieve a balance between structural stability and optimal optical performance for practical applications, we determined that H = 500 μm is the ideal substrate thickness. Fig. 5(d) demonstrates the effect of structural height Ton performance: as T increases, the FWHM decreases continuously, while the Q-factor increases gradually. This influence of structural height T on the resonance peak and FWHM underscores the importance of structural height T in metasurface design. By modifying the structural height, we can enhance the transmission efficiency and resonance characteristics of the metasurface to suit various application needs. For a high-Q sensor, a height T of 200 μm was chosen.

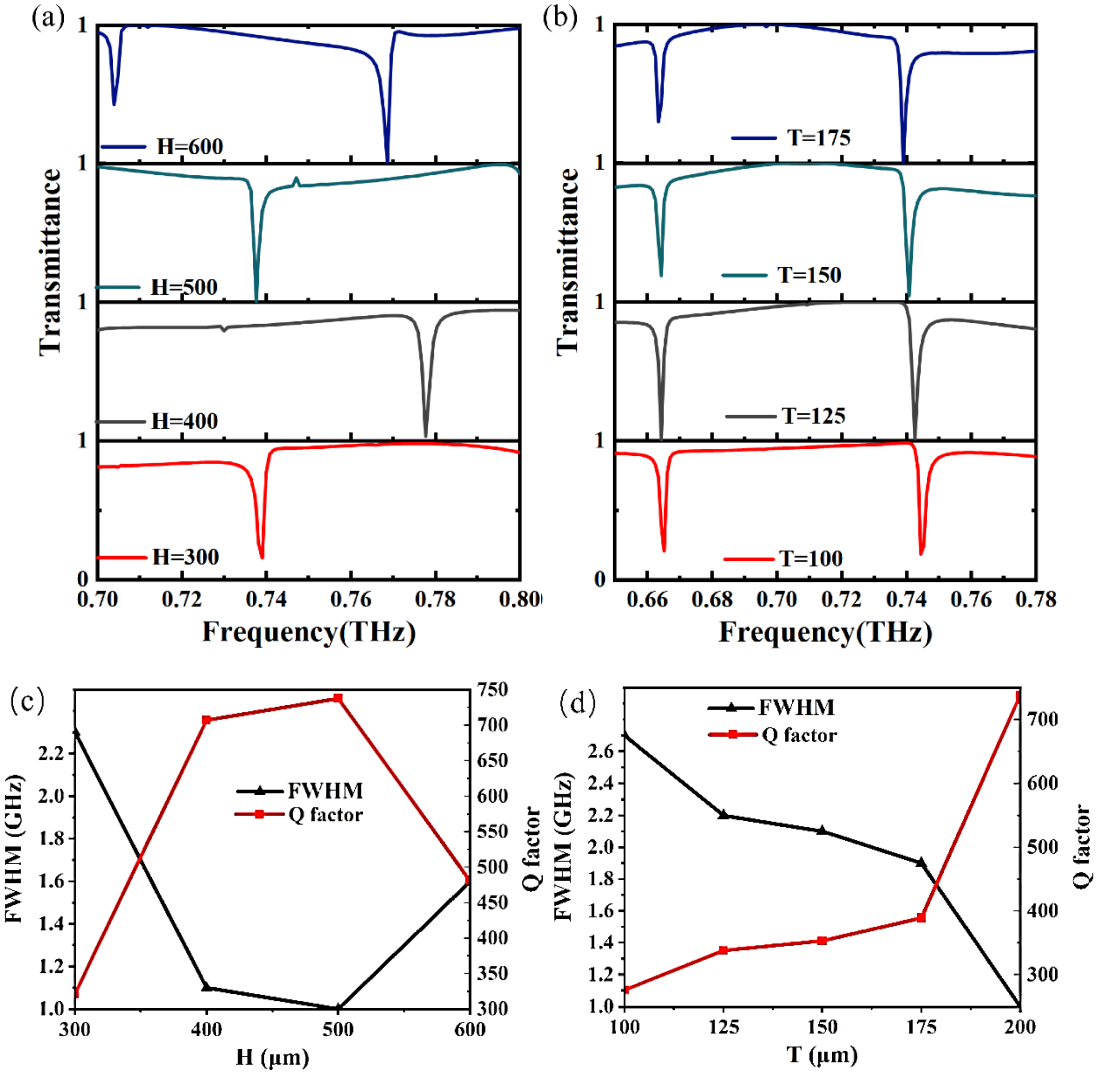

Fig. 4. Illustrates how the thickness of the metasurface substrate H and the thickness of the structure T influence the transmission spectrum of the metasurface; (a) shows the transmission spectrum in relation to varying substrate thickness H; (b) displays the transmission spectrum based on different structure thicknesses T; (c) presents the Q-f'actor associated with various substrate thicknesses H of the metasurface; (d) shows the Q-f'actor linked to different structure thicknesses T of the metasurface (colour online)

To evaluate how the metasurface responds to variations in the refractive index of the analyte, samples with different refractive indices were applied to the surface of the structure. Fig. 5(a) illustrates the transmission spectrum of the metasurface as the refractive index n of the analyte changes from 1.0 to 2.0. As *n* increases, the resonance peak exhibits a significant linear red shift, demonstrating that changes in the analyte's refractive index can effectively influence the resonance properties of the metasurface. The relationship between the change in resonance frequency and the change in refractive index is described by the equation $S = \Delta f / \Delta n$. We performed a linear regression analysis using the equation $y=kx+b$, where k represents the sensitivity, indicating how the metasurface responds to varying refractive index conditions. The fitting results, presented in Fig. 5(b), reveal that the theoretical sensitivity of this sensor is 51.31 GHz/RIU.

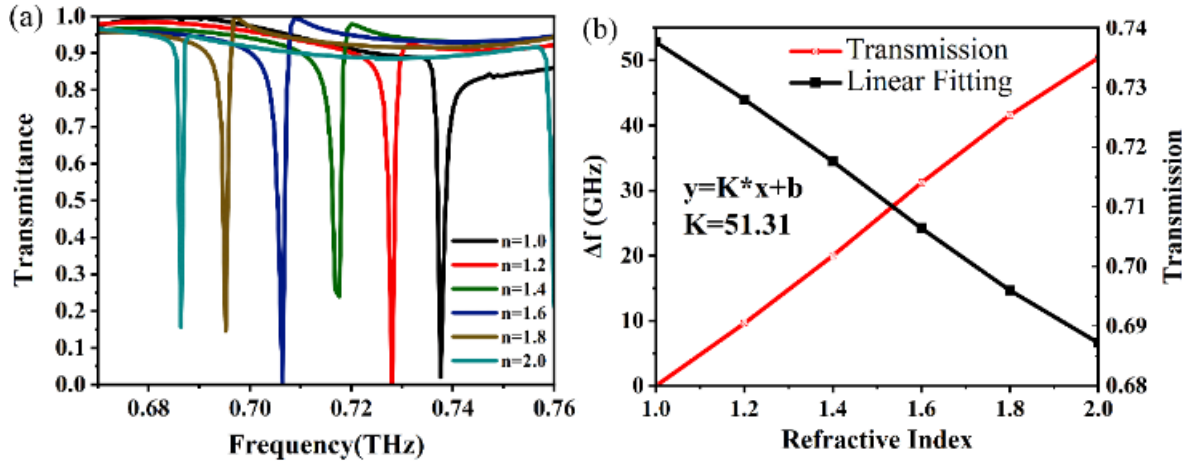

Fig. 5. Sensory performance analysis of metasurface sensors. (a) Response of metasurface structures to changes in analytes. (b) Sensitivity fitting curves of metasurface structures (colour online)

Utilizing the overall design of the metasurface shown in Fig. 1 (a) and the unit cell structure model depicted in Fig. 1 (b), we selected aluminum oxide as the material and performed iterative optimization of key geometric dimensions through parametric scanning to develop a high-performance metasurface sensor. The dielectric constant of aluminum oxide is 8.41. The optimized parameters for the aluminum oxide metasurface structure are as follows: period P_1 = 300 μm, P_2 = 400 μm, substrate thickness H = 500 μm, structure thickness T = 250 μm, short axis R_1 = 80 μm, and long axis R_2 = 90 μm for the two elliptical structures. To evaluate the performance of the metasurface, we employed the time-domain finite integral method, applying periodic boundary conditions in the x and y directions and an open boundary condition in the z direction. The electric field was oriented along the y direction, with terahertz waves incident perpendicularly on the metasurface. The transmission spectrum of the metasurface is illustrated in Fig. 6.

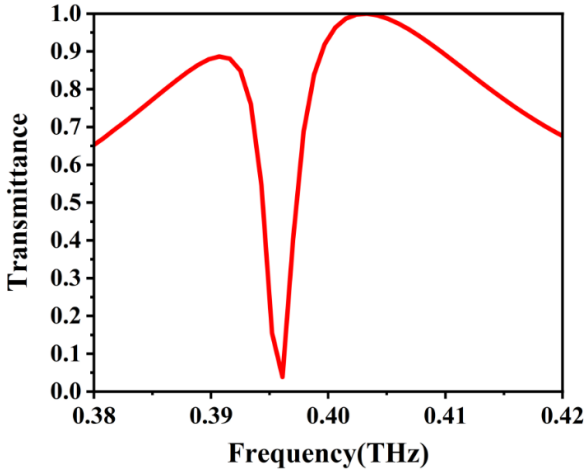

Fig. 6. Transmittance spectrum of aluminum oxide metasurface (colour online)

We created a distribution map of the near-field energy of the metasurface, as illustrated in Fig. 7. The electric field energy distribution is shown in Fig. 7 (a) and Fig. 7 (b). Fig. 7 (a) indicates that the electric field energy is primarily concentrated in the spaces between the nanocolumns. In Fig. 7 (b), it is evident that the electric field is not only focused on the nanocolumns but also exhibits significant enhancement at the top and bottom edges of these columns. The magnetic field energy distribution is presented in Fig. 7 (c) and Fig. 7 (d). These figures reveal that the magnetic field is mainly concentrated at the four corners of the elliptical structure, indicating a strong magnetic field response in that area. The distribution of both electric and magnetic fields in the metasurface demonstrates a notable local enhancement of the electromagnetic field in the near-field region, which increases the metasurface's sensitivity to variations in the environmental refractive index, thereby improving the performance of the metasurface sensor.

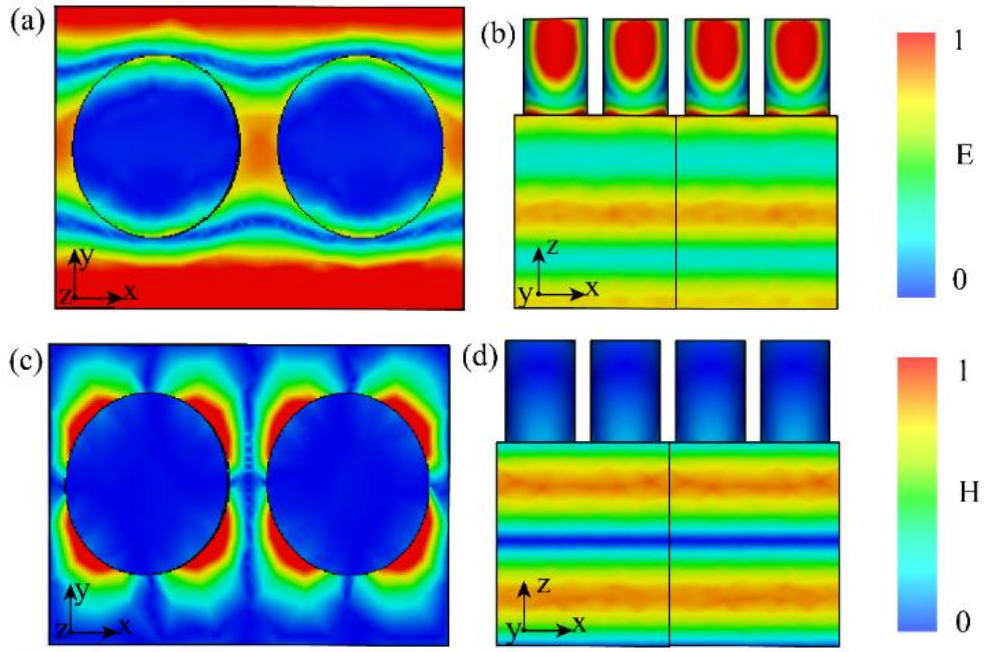

Fig. 7. Metasurface near-field energy distribution map (a) x-y plane metasurface electric field energy distribution. (b) x-z plane metasurface electric field energy distribution map. (c) x-y plane metasurface magnetic field energy distribution (d) x-z plane metasurface magnetic field energy distribution map (colour online)

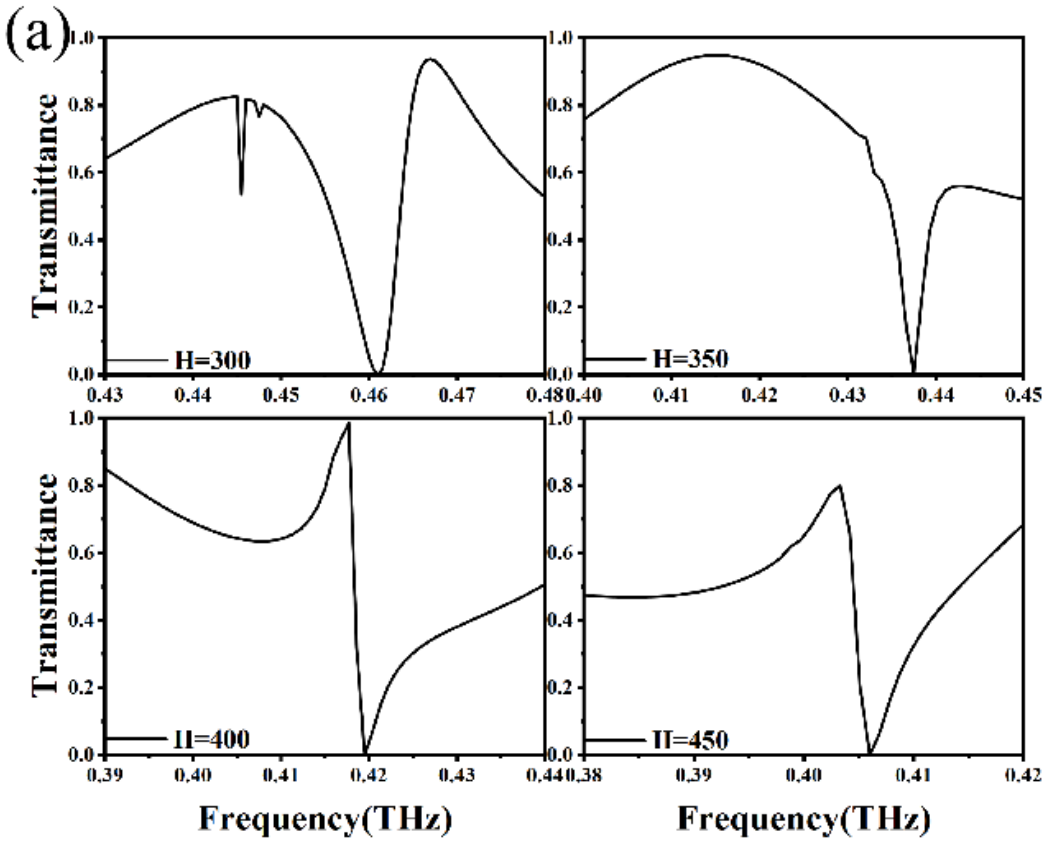

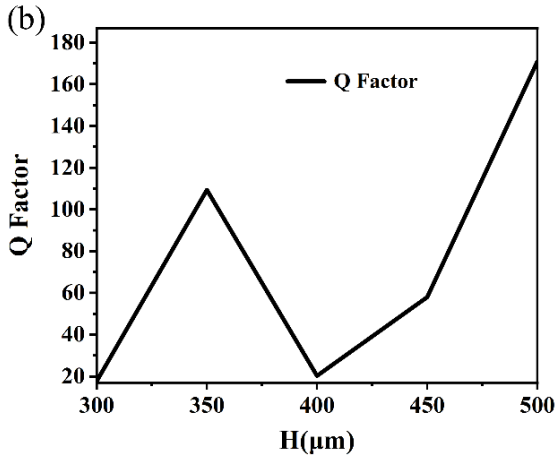

Fig. 8. Performance analysis of metasurfaces under different H conditions (a) Transmission spectrum of metasurfaces as a function of substrate thickness H; (b) Q-factor of metasurfaces under different substrate thicknesses H

We analyzed the transmission spectra of the metasurface structure with varying substrate thicknesses *H*. As illustrated in Fig. 8 (a), as the substrate thickness H increases, the peak transmission value of the metasurface remains constant, while the transmission peak shifts toward longer wavelengths. Fig. 8 (b) depicts the correlation between *H* and the Q-factor. The figure shows that the Q-factor generally increases with increasing, except at $H = 350$ μm. The Q-factor reaches its highest value of 170.87 when $H = 500$ μm. Consequently, to optimize the performance of the metasurface, a substrate thickness of $H = 500$ μm is selected.

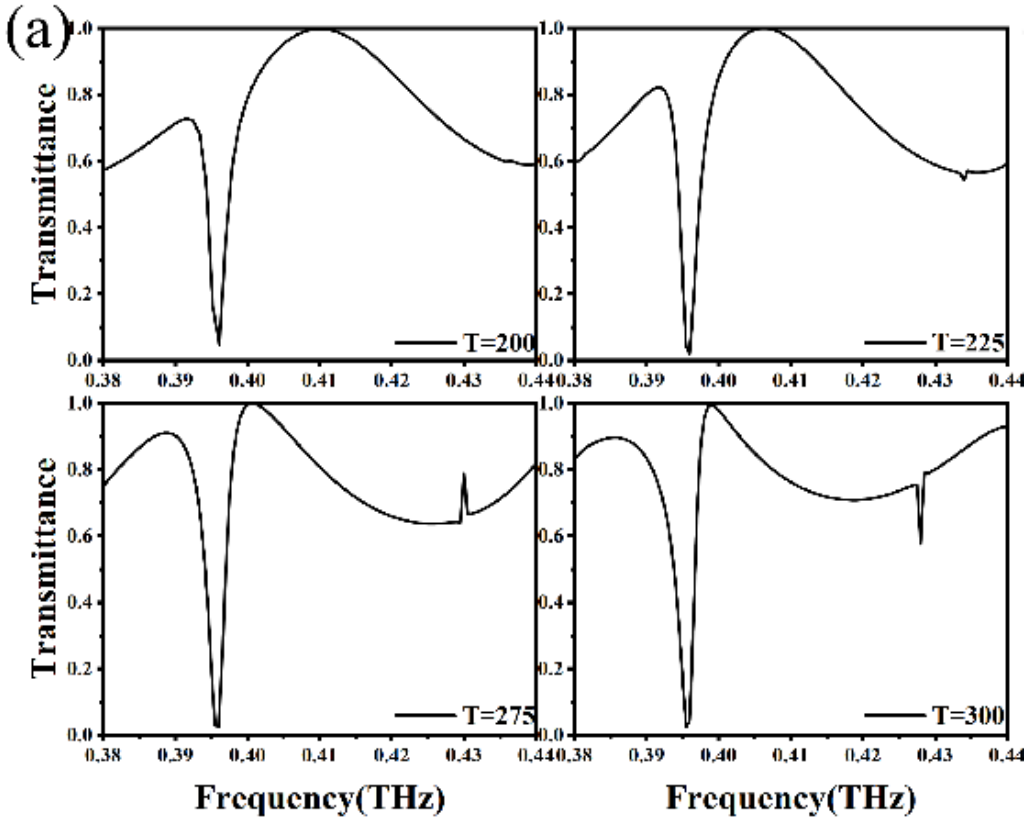

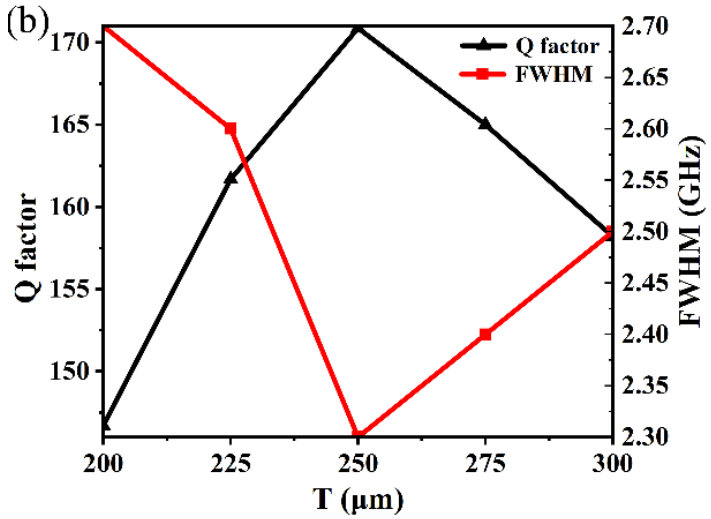

Fig. 9. Performance analysis of metasurfaces at different T values (a) Transmission spectrum of metasurfaces at different T values; (b) Q-factor of metasurfaces at different T values (colour online)

Fig. 9 illustrates the transmission spectrum of the metasurface at various structural thicknesses T. The data reveal that as the structural thickness increases, both the position and peak value of the transmission peak remain nearly constant, indicating that structural thickness has minimal impact on the resonance frequency of the metasurface. Fig. 9 (b) shows the relationship between T and the FWHM and Q-factor. The figure indicates that at T = 250 μm, which serves as a turning point, the FWHM of the transmission peak initially decreases and then increases as T continues to rise. According to the equation Q= f / FWHM, the Q-factor of the metasurface also exhibits a pattern of first increasing and then decreasing with increasing T. At T = 250 μm, the Q-factor reaches its peak at approximately 170.87, demonstrating that variations in structural thickness significantly affect the Q-factor. Consequently, to achieve a high-Q metasurface sensor, T = 250 μm is selected.

The selection of the short axis R1 for the metasurface requires careful consideration of the precision needed for material preparation and the size of the metasurface unit periodicity. Consequently, the maximum feasible value for R1 is 80 μm.

Fig. 10(a) displays the transmission spectra of the metasurface for various R1 values. The figure indicates that variations in the short axis R1 do not significantly affect the position of the transmission peak.

Fig. 10(d) illustrates the trend of changes in the Q-factor associated with different R1 values of the metasurface. As R1 increases, the Q-factor also rises, peaking at 80 μm. Therefore, to achieve a metasurface sensor with the optimal Q-factor, R1 is set to 80 μm. Similarly, we analyzed the transmission spectrum of the metasurface in relation to the long axis R2, as illustrated in

Fig. 10(b). The figure shows that as R2 increases, the transmission peak gradually shifts toward the red end of the spectrum, although the change in peak value is minimal.

Fig. 10(e) presents the trends of changes in the Q-factor and FWHM for different R2 values. It is evident that as R2 increases, the FWHM initially rises and then falls, while the corresponding Q-factor first decreases and then gradually increases. The Q-factor reaches its highest value of 170.87 when R2 is 90 μm. Therefore, to achieve a high-Q metasurface sensor, R2 is chosen to be 90 μm.

To evaluate the refractive index sensitivity, we varied the refractive index n of the surrounding medium from 1.0 to 2.0. Fig. 10 (c) illustrates how the transmission spectrum of the metasurface changes as the refractive index n varies from 1.0 to 2.0. As n increases, the transmission peak curve of the supersurface undergoes redshift. Fig. 10 (f) provides additional data on the sensitivity of the metasurface. According to Equations $S = \Delta f / \Delta n$, the variation in resonance frequency is directly proportional to the refractive index. A linear fit was performed using the equation $y = kx + b$, where k represents the sensitivity. The fitting results indicate that the theoretical sensitivity of the metasurface is 6.93 GHz/RIU.

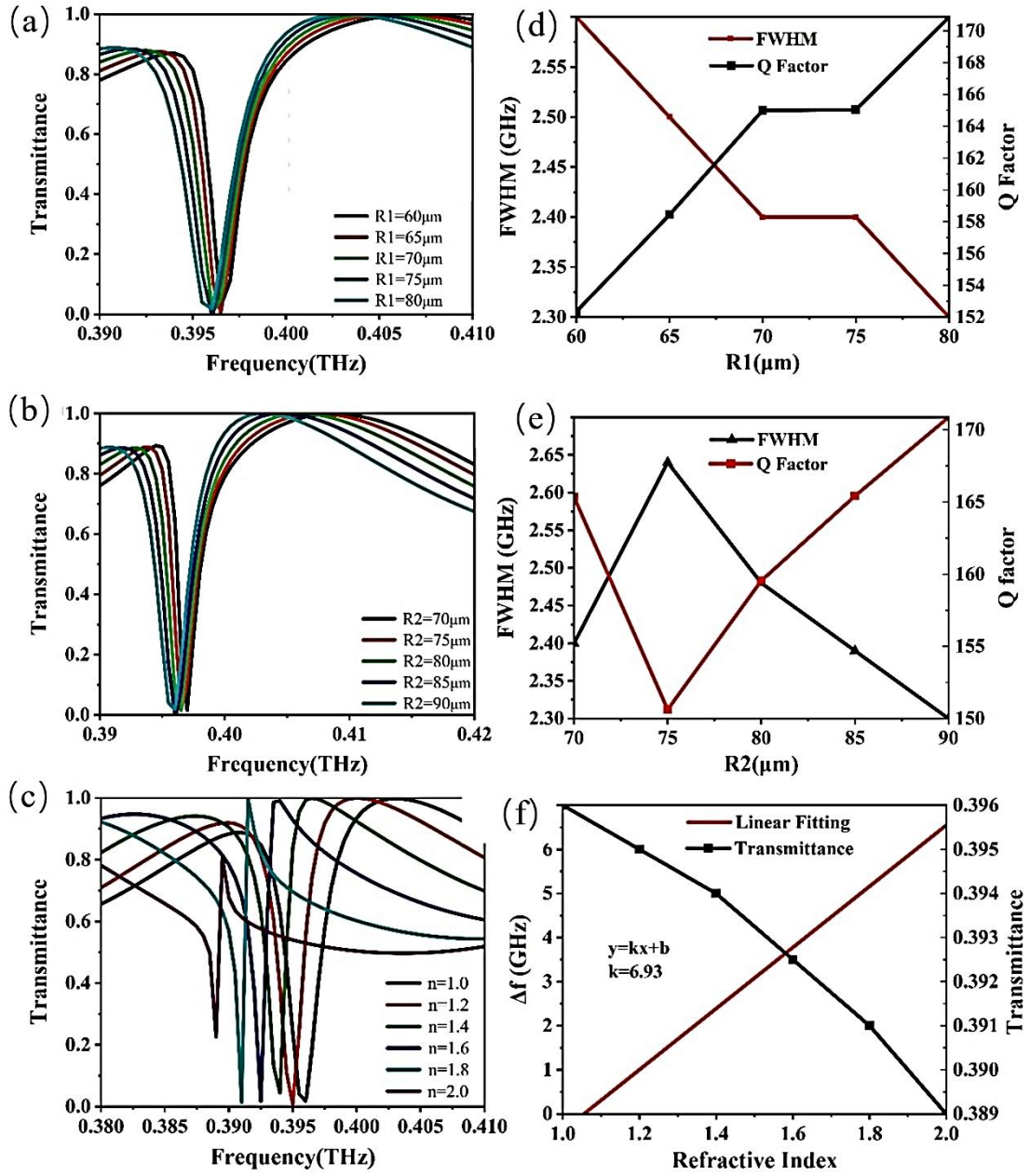

Fig. 10. Performance analysis of metasurfaces (a) Transmission spectra of metasurfaces under different R_1 conditions. (b) Transmission spectra of metasurfaces under different R_2 conditions. (c) Transmission spectra of metasurfaces under different refractive index conditions. (d) Q-factor of metasurfaces under different R_1 conditions (e) Q-factor of metasurfaces under different R_2 conditions. (f) Sensitivity fitting curves of metasurfaces (colour online)

Table 1. Comparison of core performance parameters of terahertz metasurface sensors under optimal structures of two materials

Metasurface type	Quality factor	Sensitivity (GHz/RIU)
photopolymer resin	737.6	51.31
aluminum oxide	170.87	6.931

Table 1 compares the core performance parameters of terahertz metasurface sensors with optimized structures using photopolymer resin and aluminum oxide materials. The test results show that the photopolymer resin metasurface sensor achieves a quality factor of 737.6 and a sensitivity of 51.31 GHz/RIU, whereas the alumina-based metasurface sensor exhibits a Q-factor of only 170.87 and a sensitivity of just 6.931 GHz/RIU. This significant disparity

in performance indicates that low-refractive-index photosensitive polymers, due to their inherent material properties, offer distinct advantages in enhancing both the quality factor and sensing sensitivity of terahertz metasurface sensors.

The research frontier for metasurfaces is rapidly expanding beyond static wavefront manipulation, pivoting towards dynamic, intelligent, and multifunctional flat optics that will redefine photonic systems [37-45]. A primary thrust will be the development of actively tunable metasurfaces. While current devices are largely passive, future research will focus on integrating dynamic materials such as phase-change materials (e.g., GST), transparent conductive oxides (e.g., ITO), and two-dimensional materials like graphene [46-70]. By applying external stimuli — electrical, optical, or thermal — these "smart" surfaces will enable real-time control over amplitude, phase, and polarization, unlocking applications in LiDAR, adaptive optics, and next-generation holographic displays. Concurrently, the drive towards nonlinear metasurfaces will intensify. By engineering resonances in materials with high nonlinear susceptibility, such as lithium niobate or certain III-V semiconductors, we can create compact sources of coherent light, perform frequency conversion with unprecedented efficiency, and explore quantum optical phenomena on a chip-scale platform. This will be crucial for advancing integrated quantum photonics and on-chip signal processing [71-80].

Furthermore, the paradigm of metasystem design is set to be revolutionized by deep learning and inverse design methodologies. Instead of relying solely on intuitive, parameterized sweeps, researchers will increasingly use AI-driven models to discover complex, non-intuitive nanostructures that optimally fulfill multiple, often conflicting, performance criteria — such as extreme bandwidth, wide angle operation, and high efficiency simultaneously [81-90]. This co-design approach, integrating the metasurface directly with electronic control circuits and light sources, will be essential for creating truly monolithic, wafer-scale meta-optical systems. Finally, we anticipate a significant push towards heterogeneous integration, where metasurfaces are no longer standalone components but are seamlessly bonded onto diverse platforms like CMOS image sensors for computational imaging, onto optical fibers for endoscopic applications, and even onto semiconductor lasers for beam shaping and mode locking. This convergence of active tunability, nonlinear optics, and AI-augmented design will ultimately transition metasurfaces from laboratory curiosities into indispensable, mass-producible technologies that underpin future advancements in communications, sensing, and computing [91-105].

The field of metasurface-based biomolecular detection is poised for transformative advancements, moving beyond conventional sensing paradigms to enable unprecedented sensitivity, miniaturization, and functional integration. Future research will likely focus on several key frontiers to translate laboratory breakthroughs into practical, impactful technologies. Firstly, the innovation in material platforms and resonance mechanisms will continue to be a primary driver. All-dielectric metasurfaces, leveraging high-quality-factor (high-Q) resonances such as quasi-bound states in the continuum (q-BICs) and Fano resonances, have demonstrated remarkable potential due to their low optical loss and significant near-field enhancement. The recent demonstration of nonlocal q-BICs that create a uniform and significant near-field enhancement outside the nanostructures, enabling a 35-fold improvement in the detection limit for a breast cancer biomarker, highlights a crucial direction: engineering near-field distribution to maximize light-matter interaction with target biomolecules in the sensing volume, rather than confining energy within the sensor material itself. Furthermore, hybrid metasurfaces that synergistically combine the high sensitivity of plasmonic metals with the high Q factors of dielectrics present a powerful strategy. These systems can support multiple resonance modes, with dielectric-dominated q-BICs excelling in bulk refractive index sensitivity and metal-dominated modes offering superior surface affinity, thereby providing a versatile sensing platform. The integration of dynamic, tunable materials like graphene and transition metal dichalcogenides (TMDCs) will further allow for active, reconfigurable sensors. For instance, graphene's Fermi level tunability has been exploited for electro-optic modulation in sensors, and its combination with metasurfaces can lead to reversible biosensing capabilities, as preliminarily shown in the terahertz regime.

Secondly, the paradigm of sensing itself is evolving from simple spectral shift monitoring towards multidimensional and intelligence-augmented information extraction. The integration of hyperspectral imaging with dielectric metasurfaces represents a monumental leap, transforming a sensor into a high-throughput analytical platform. This approach can generate millions of spectra from a single CMOS image, allowing for digital sensing via pixel-level statistical analysis and pushing the detection limit to the level of few molecules per square micrometer. The concept of "multiresonant sensors" (MRS) and barcode-based sensing, where a single metasurface is engineered with a spatial gradient of resonance wavelengths, enables spectral information retrieval from a single-wavelength intensity image, drastically simplifying the required instrumentation. Concurrently, the analysis of multiple parameters—including resonance frequency, amplitude, phase, and linewidth—provides a rich, multidimensional dataset that can significantly enhance specificity and accuracy in complex biological environments, as demonstrated in flexible terahertz metasurfaces for distinguishing cancerous cells. The future will undoubtedly see a deeper convergence of metasurface data with artificial intelligence (AI) and machine learning algorithms. AI will be instrumental in deconvoluting complex spectral patterns, identifying subtle fingerprints of specific biomarkers, and compensating for non-specific binding effects, ultimately leading to robust and intelligent diagnostic systems [106-116].

Finally, the trajectory points strongly towards system-level integration and the tackling of real-world clinical challenges. The ultimate goal is the development of portable, low-cost, and point-of-care (POC) devices. Progress in miniaturization is already evident, with the successful integration of metasurface chips into portable, multi-well plate readers for rapid and ultra-sensitive screening of cancer biomarkers like AFP, CEA, and CA125 directly from clinical serum samples. The use of nanozymes in conjunction with metasurface plasmon sensors (Nano-ELISPR) exemplifies a trend toward simplifying assay workflows while amplifying signals, achieving detection limits in the femtomolar range. Looking ahead, the fusion of sensing and communication functionalities on a single metasurface platform is an emerging frontier. Research into reconfigurable intelligent surfaces (RIS) for 5G/6G networks could be harnessed to create devices that not only sense biomarkers but also wirelessly transmit data, enabling the development of autonomous, networked health monitoring systems. Overcoming the challenges of environmental stability, reproducible mass-production of ultra-precisely nanostructured surfaces, and validation with large sets of real clinical samples will be the critical steps that determine the transition of these remarkable laboratory innovations into tools that can truly redefine early disease diagnostics and personalized medicine.

5. Conclusions

In this study, we conducted simulation analyses of biosensors utilizing photopolymer resin and aluminum oxide materials. The results indicate that the metasurface biosensor constructed from photopolymer resin exhibits a sharp resonance peak at 0.7376 THz, with a theoretical Q-factor of 737.6 and a theoretical sensitivity of 51.31 GHz/RIU. In contrast, the matasurface biosensor employing aluminum oxide displays a Fano resonance peak at 0.3961 THz, with a theoretical Q-factor of 170.87 and a theoretical sensitivity of 6.93 GHz/RIU. The simulation results reveal that the photopolymer resin demonstrates greater stability in resonance effects and significantly higher sensitivity compared to aluminum oxide. Consequently, photopolymer resin is considered more advantageous for application as a metasurface biosensor.

References

[1] S. Bodrov, A. Murzanev, A. Korytin, A. Stepanov, Optics Letters **46**(23), 5946 (2021).
[2] H. Kaur, H. S. Singh, Optik **250**, 168339 (2022).
[3] M. Zhang, Q. Cheng, B. Wang, L. Yang, J. Wang, R. Wu, W. Hou, Optics Communications **507**, 127519 (2022).
[4] G. Gallot, S. P. Jamison, R. W. McGowan, D. Grischkowsky, J. Opt. Soc. Am. B **17**(5), 851 (2000).
[5] M. Khorasaninejad, W. T. Chen, A. Y. Zhu, J. Oh, R. C. Devlin, D. Rousso, F. Capasso, Nano Letters **16**(7), 4595 (2016).
[6] Z. Shen, K. Zhu, D. M. O'Carroll, ACS Photonics **5**(4), 1215 (2018).
[7] H. Pahlevaninezhad, M. Khorasaninejad, Y. W. Huang, Z. Shi, L. P. Hariri, D. C. Adams, A. Zhu, C. W. Qiu, F. Capasso, M. J. Suter, Conference on Lasers and Electro-Optics (CLEO), 1 (2018).
[8] X. Xu, Y. Ying, Y. Li, Procedia Engineering **25**, 67 (2011).
[9] K. B. Alici, IEEE Transactions on Nanotechnology **13**(2), 216 (2014).
[10] W. Xu, L. Xie, J. Zhu, L. Tang, R. Singh, C. Wang, Y. Ma, H.-T. Chen, Y. Ying, Carbon **141**, 247 (2019).
[11] J. Hu, F. Safir, K. Chang, S. Dagli, H. B. Balch, J. M. Abendroth, J. Dixon, P. Moradifar, V. Dolia, M. K. Sahoo, B. A. Pinsky, S. S. Jeffrey, M. Lawrence, J. A. Dionne, Nature Communications **14**(1), 4486 (2023).
[12] A. Krasnok, M. Tymchenko, A. Alù, Materials Today **21**(1), 8 (2018).
[13] K. R. McIntire, Cancer Research **40**(8_Part_2), 3083 (1980).
[14] L. Wesemann, J. Rickett, T. J. Davis, A. Roberts, ACS Photonics **9**(5), 1803 (2022).
[15] S. Nourinovin, A. Alomainy, IEEE MTT-S International Microwave Biomedical Conference (IMBioC), 236 (2022).
[16] L. Liu, T. Li, Z. Liu, F. Fan, H. Yuan, Z. Zhang, S. Chang, X. Zhang, Optics Express **11**(5), 2416 (2020).
[17] C. M. Soukoulis, M. Wegener, Science **330**(6011), 1633 (2010).
[18] S. Zhang, C. L. Wong, S. Zeng, R. Bi, K. Tai, K. Dholakia, M. Olivo, Nanophotonics **10**(1), 259 (2021).
[19] A. Krasnok, G. Palermo, K. V. Sreekanth, G. Strangi, S. Vellucci, EPJ Applied Metamaterials **7**, 11 (2020).
[20] Z. Huang, M. Wang, Y. Li, J. Shang, K. Li, W. Qiu, J. Dong, H. Guan, Z, Chen, H. Lu, Nanotechnology **32**(32), 325207 (2021).
[21] J. Zhang, N. Mu, L. Liu, J. Xie, H. Feng, J. Yao, T. Chen, W. Zhu, Biosensors and Bioelectronics **185**, 113241 (2021).
[22] C. Zhang, T. Xue, J. Zhang, L. Liu, J. Xie, G. Wang, J. Yao, W. Zhu, X. Ye, Nanophotonics **11**(1), 101 (2022).
[23] N. Meinzer, W. L. Barnes, I. R. Hooper, Nature Photonics **8**(12), 889 (2014).
[24] K. Watanabe, M. Iwanaga, Nanophotonics **12**(1), 99 (2023).
[25] M. Li, Q. Ma, A. Luo, W. Hong, Optics and Laser Technology **154**, 108252 (2022).
[26] J. Wang, J. Kuhne, T. Karamanos, C. Rockstuhl,

S. A. Maier, A. Tittl, Advanced Functional Materials **31**, 2104652 (2021).
[27] M. Iwanaga, Biosensors **11**(2), 33 (2021).
[28] Y. Jahani, E. R. Arvelo, F. Yesilkoy, K. Koshelev, C. Cianciaruso, M. De Palma, Y. Kivshar, H. Altug, Nature Communications **12**(1), 3246 (2021).
[29] K. Liu, R. Zhang, Y. Liu, X. Chen, K. Li, Biomed. Opt. Express **12**(3), 1559 (2021).
[30] A. E. Cetin, Z. A. Kocer, S. N. Topkaya, Z. A. Yazici, Sensors and Actuators B: Chemical **344**, 130301 (2021).
[31] K. Yang, J. Li, M. Lamy de la Chapelle, G. Huang, Y. Wang, J. Zhang, D. Xu, J. Yao, X. Yang, W. Fu, Biosensors and Bioelectronics **175**, 112874 (2021).
[32] H. Yao, Z. Sun, L. Liang, X. Yan, Y. Wang, M. Yang, X. Hu, Z. Wang, Z. Li, M. Wang, C. Huang, Q. Yang, Z. Tian, J. Yao, Photonics Research **11**(5), 858 (2023).
[33] Q. Xie, L. Guo, Z. Zhang, P. Gao, M. Wang, F. Xia, K. Zhang, P. Sun, L. Dong, M. Yun, Applied Surface Science 604, 154575 (2022).
[34] M. Ye, K. B. Crozier, Optics Express **28**(12), 18479 (2020).
[35] S.-H. Lee, J.-H. Choe, C. Kim, S. Bae, J.-S. Kim, Q.-H. Park, M. Seo, Sensors and Actuators B: Chemical **310**, 127841 (2020).
[36] A. Alipour, A. Farmani, A. Mir, Plasmonics **15**(6), 1935 (2020).
[37] J. Lyu, L. Huang, L. Chen, Y. Zhu, S. Zhuang, Photonics Research **12**(2), 194 (2024)
[38] L. Chen, Y. Song, D. C. Y. Lim, Y. Zhu, S. Zhuang, R. Singh, TrAC Trends in Analytical Chemistry **193**, 118416 (2025).
[39] Z. Y. Luo, Y. Q. Ding, F. L. Peng, G. Wei, Y. Wang, S. T. Wu, Opto-Electronic Advances **7**(10), 240039 (2024).
[40] S. S. Li, Y. N. Fang, J. F. Wang, Opto-Electronic Science **3**(7), 240011 (2024).
[41] M. W. Liang, D. Z. Lu, Y. G. Ma, Opto-Electronic Engineering **51**(8), 240068 (2024).
[42] Naglaa AbdelAll, Mohamed Almokhtar, Ghada Khouqeer, Israa Abood, Sayed El. Soliman, Advanced Quantum Technologies **7**(9), 2400050 (2024).
[43] Valeria Istokskaia, Benoit Lefebvre, Roberto Versaci, Dragana B. Dreghici, Domenico Doria, Filip Grepl, Veronika Olšovcová, Francesco Schillaci, Stanislav Stanček, Maksym Tryus, Andriy Velyhan, Daniele Margarone, Lorenzo Giuffrida, High Power Laser Science and Engineering **12**, 05000e57 (2024).
[44] Cade Peters, Andrew Forbes, Advanced Photonics **6**(4), 040501 (2024).
[45] S. X. Zhang, H. Li, C. Z. Fan, Z. C. Zeng, C. Xiong, J. Wu, Z. J. Yan, D. M. Liu, Q. Z. Sun, Opto-Electronic Advances **7**(12), 240119 (2024).
[46] S. Rane, S. Prabhu, D. R. Chowdhury, Opto-Electronics Science **3**(11), 230049 (2024).
[47] H. Yang, H. R. He, Y. Q. Hu, H. G. Duan, Opto-Electron Engineering **51**(8), 240168 (2024).
[48] Shilin Liu, Wenhan Cao, Shizeng Jiang, Lianhao He, Fangting Lin, Xiaoyong He, Advanced Quantum Technologies **7**(4), 2300386 (2024).
[49] Jianmei Shi, Chengao Yang, Yihang Chen, Tianfang Wang, Hongguang Yu, Juntian Cao, Zhengqi Geng, Zhiyuan Wang, Haoran Wen, Hao Tan, Yu Zhang, Dongwei Jiang, Donghai Wu, Yingqiang Xu, Haiqiao Ni, Zhichuan Niu, High Power Laser Science and Engineering **12**, 04000e42 (2024).
[50] Jian Zhang, Haochun Zhang, Gang Zhang, Frontiers of Physics **19**(2), 23204 (2024).
[51] Tao Hou, Yixiao Ge, Shuwen Xue, Huanyang Chen, Frontiers of Physics **19**(3), 32201 (2024).
[52] Joonhyuk Seo, Jaegang Jo, Joohoon Kim, Joonho Kang, Chanik Kang, Seong-Won Moon, Eunji Lee, Jehyeong Hong, Junsuk Rho, Haejun Chung, Advanced Photonics **6**, 066002 (2024).
[53] Y. C. Wu, Q. P. Yang, B. T. Shen, Y. S. Tao, X. G. Zhang, Z. H. Tao, L. W. Xing, Z. F. Ge, T. T. Li, B. W. Bai, H. W. Shu, X. J. Wang, Opto-Electronic Science **3**(8), 240012 (2024).
[54] Xin Ge Zhang, Qiu Cen Hu, Qi Yang Li, Zhixiang Huang, Liang Xu, Yi Quan, Qian Zhu, Bo Yuan Wang, Xiao Xiao Chen, Tie Jun Cui, Wei Xiang Jiang, Photonics Research **12**(11), 2660 (2024).
[55] Z. J. Yu, M. X. Li, Z. Y. Xing, H. Mao, H. Cai, Q. Ma, W. Q. Ren, J. Zhu, C. Zhang, Opto-Electronic Science **3**(9), 240016 (2024).
[56] H. X. Wang, Y. L. He, H. W. Zhu, H. Dong, S. N. Wang, Opto-Electronic Engineering **51**(8), 240095 (2024).
[57] Bakr Ahmed Taha, Ali J. Addie, Adawiya J. Haider, Vishal Chaudhary, Retna Apsari, Ajeet Kaushik, Norhana Arsad, Advanced Quantum Technologies **7**(3), 2300414 (2024).
[58] Lian Zhou, Haipeng Lou, Zejiang Deng, Xiong Qin, Jiayi Pan, Yuanfeng Di, Chenglin Gu, Daping Luo, Wenxue Li, High Power Laser Science and Engineering **12**, 03000e23 (2024).
[59] Md Sadman Sakib Rahman, Aydogan Ozcan, Advanced Photonics **6**, 050500 (2024).
[60] Linkang Han, Qilin Duan, Junliang Duan, Shan Zhu, Shiming Chen, Yuhang Yin, Huanyang Chen, Frontiers of Physics **19**(3), 32206 (2024).
[61] Hongxin Zeng, Xuan Cong, Shiqi Wang, Sen Gong, Lin Huang, Lan Wang, Huajie Liang, Feng Lan, Haoyi Cao, Zheng Wang, Weipeng Wang, Shixiong Liang, Zhihong Feng, Ziqiang Yang, Yaxin Zhang, Tie Jun Cui, Photonics Research **12**, 1004 (2024).
[62] Bowen Zeng, Chenxia Li, Bo Fang, Zhi Hong, Xufeng Jing, Photonics Research **12**, 61 (2024).
[63] Jingwen Zhou, Yaling Yin, Jihong Tang, Yong Xia,

Jianping Yin, Frontiers of Physics **19**(5), 52202 (2024).
[64] J. C. Zhang, M. K. Chen, Y. B. Fan, Q. M. Chen, S. F. Chen, J. Yao, X. Y. Liu, S. M. Xiao, D. P. Tsai, Opto-Electronics Advances **7**(2), 230171 (2024).
[65] Y. N. Zhang, Y. G. Chen, T. Wang, Opto-Electronics Advances **7**(4), 230194 (2024).
[66] Muhib Ullah, Said Mikki, Advanced Quantum Technologies **7**(7), 2400007 (2024).
[67] Zaharit Refaeli, Gilad Marcus, Yariv Shamir, High Power Laser Science and Engineering **12**, 02000e18 (2024).
[68] Zhanlei Hao, Haojie Chen, Yuhang Yin, Cheng-Wei Qiu, Shan Zhu, Huanyang Chen, Frontiers of Physics **19**(4), 42202 (2024)
[69] Che-Yung Shen, Jingxi Li, Yuhang Li, Tianyi Gan, Langxing Bai, Mona Jarrahi, Aydogan Ozcan, Advanced Photonics **6**, 056003 (2024).
[70] A. M. Berhe, K. As'ham, I. Al-Ani, H. T. Hattori, A. E. Miroshnichenko, Opto-Electronics Advances **7**(5), 230181 (2024).
[71] Chenglong Zheng, Hui Li, Jingyu Liu, Mengguang Wang, Huaping Zang, Yan Zhang, Jianquan Yao, Photonics Research **12**, 514 (2024).
[72] T. Nan, H. Zhao, J. Y. Guo, X. Wang, H. Tian, Y. Zhang, Opto-Electronics Science **3**(5), 230052 (2024).
[73] Chun-Lin Zhang, Kai-Xin Hu, Jie Zhang, Ji Cao, Shou Zhang, Hong-Fu Wang, Advanced Quantum Technologies 7(10), 2400165 (2024).
[74] Y. Chen, S. M. Zhang, Y. Tian, C. X. Li, W. L. Huang, Y. X. Liu, Y. X. Jin, B. Fang, Z. Hong, X. F. Jing, Opto-Electronic Advances **7**(8), 240095(2024)
[75] H. J. Zhan, M. N. Gu, Y. Tian, H. Z. Feng, M. M. Zhu, H. M. Zhou, Y. X. Jin, Y. Tang, C. X. Li, B. Fang, Z. Hong, X. F. Jing, L. Wang, Opto-Electronic Advances **8**(7), 240315(2025).
[76] P. Gong, A. B. Du, F. Zhang, M. B. Pu, T. J. Tang, L. T. Li, X. G. Luo, Opto-Electronic Engineering **51**(8), 240040 (2024).
[77] Rodrigo Martín-Hernández, Lorenz Grünewald, Luis Sánchez-Tejerina, Luis Plaja, Enrique Conejero Jarque, Carlos Hernández-García, Sebastian Mai, Photonics Research **12**, 1078 (2024).
[78] Jie Jiang, Bo Fang, Chenxia Li, Zhi Hong, Xufeng Jing, Photonics Research **11**, 1738 (2023).
[79] S. Y. Xiang, Z. W. Song, Y. H. Zhang, X. X. Guo, Y. N. Han, Y. Hao, Opto-Electronic Engineering **51**(7), 240101 (2024).
[80] Xinqin Meng, Chengbing Qin, Xilong Liang, Guofeng Zhang, Ruiyun Chen, Jianyong Hu, Zhichun Yang, Jianzhong Huo, Liantuan Xiao, Suotang Jia, Frontiers of Physics **19**(5), 53601 (2024).
[81] Léo J. Roche, Fridtjof Betz, Yuhui Yang, Imad Limame, Ching-Wen Shih, Sven Burger, Stephan Reitzenstein, Advanced Quantum Technologies **7**(12), 2400195 (2024).
[82] Yixin Liu, Ying Tian, Chenxia Li, Bo Fang, Jianjun Liu, Zhi Hong, Xufeng Jing, Photonic Research **12**, 2344 (2024).
[83] X. Jing,X. Gui, P. Zhou, Z. Hong, Journal of Lightwave Technology **36**(12), 2322 (2018).
[84] R. Xia, X. Jing, X. Gui, Y. Tian, Optics Materials Express **7**(3), 977 (2017).
[85] J. Zhao, X. Jing, W. Wang, Y. Tian, D. Zhu, G. Shi, Optics and Laser Technology **95**, 56 (2017).
[86] Q. Y. Wang, C. X. Li, B. Fang, L. Ke, J. X. Lu, X. L. Ma, Z. Hong, X. F. Jing, Journal of Lightwave Technology **41**(23), 7098 (2023).
[87] B. W. Zeng, C. X Li, H. L. Cheng, B. Fang, J. X. Lu, X. L. Ma, L. Wang, Z. Hong, X. F. Jing, Optics and Lasers in Engineering, **169**, 107723 (2023).
[88] G. H, Qin, Y. Y. Dong, P. Zhang, J. J. Liu, C. X. Li, W. K. Huang, Z. Hong, C. Y. Shen, X. F. Jing, Optics and Lasers in Engineering **160**, 107288 (2023).
[89] X. F. Jing, X. Y. Tang, Y. Tian, Z. Kong, C. X. Li, C. Y. Shen, H. Zhi, Journal of Lightwave Technology **40**(1), 136 (2022).
[90] H. L. Cheng, B. Fang, W. K. Huang, R. S. Li, C. Y. Shen, L. Ke, X. F. Jing, C. X. Li, Z. Hong, Optics and Laser Technology **156**,108520 (2022).
[91] Weimin Wang, Xufeng Jing, Jingyin Zhao, Yinyan Li, Ying Tian, Optica Applicata **47**(2),183 (2017).
[92] L. Jiang, B. Fang, Z. Yan, J. Fan, C. Qi, J. Liu, Y. He, C. Li, X. Jing, H. Gan, Z. Hong, Optics and Laser Technology **123**, 105949 (2020).
[93] L. Jiang, B. Fang, Z. Yan, C. Li, J. Fu, H. Gan, Z. Hong, X. Jing, Microwave and Optical Technology Letters **62**(6), 2405 (2020).
[94] X. Jing, Y. Xu, H. Gan, Y. He, Z. Hong, IEEE Access **7**, 144945 (2019).
[95] Yingjuan Lu, Qiang Cheng, Siran Wang, Huidong Li, Junyan Dai, zhen Zhang, Jiang Luo, Acta Optica Sinica **2**(4), 0401001 (2025).
[96] Yang Fei, Ruozhang Xing, Jing Chen, Xiujuan Zou, Shuming Wang. Acta Optica Sinica **3**(2), 0202001 (2026).
[97] Bin Yu, Quan Zhou, Li Yuan, Huageng Liang, Pavel Shcherbakov, Xuming Zhang, CAAI Transactions on Intelligence Technology, **10**(2), 337 (2025).
[98) Helong Yu, Jiuman Song, Chengcheng Chen, Ali Asghar Heidari, Yuntao Ma, Huiling Chen, Yudong Zhang, CAAI Transactions on Intelligence Technology **10**(3), 755 (2025).
[99] M. Kim, H. Kim, Photonic Sensors **15**, 250201 (2025).
[100] X. Wu, C. Zhu, Y. Wang, X. Fan, Photonic Sensors **15**(1), 250123 (2025).
[101] Yu Liang, Yanyan Dong, Yongxing Jin, Lan Ke, Chenxia Li, Xufeng Jing, Infrared Physics and Technology **127**,104441 (2022).

[102] Kexin Wang, Xin Li, Yongtian Wang, Lingling Huang. Acta Optica Sinica **2**(14), 1409004 (2025).
[103] Z. Cui, K. Wen, H. Lv, W. Liu, Y. Yu, R. Zhang, R. Liu, Photonic Sensors **15**, 250433 (2025).
[104] Guihong Qin, Yanyan Dong, Peng Zhang, Jianjun Liu, Chenxia Li, Wenkang Huang, Zhi Hong, Changyu Shen, Xufeng Jing, Optics and Lasers in Engineering **160**, 107288 (2022).
[105] Ying Chen, Peng Min, Huiling Chen, Cheng Tao, Zeye Long, Ali Asghar Heidari, Shuihua Wang, Yudong Zhang, CAAI Transactions on Intelligence Technology **10**(6), 1844 (2025).
[106] Zhuo Li, Shiliang Pu, Mengqi Ji, Feng Zeng, Bo Li, CAAI Transactions on Intelligence Technology, **10**(1), 193 (2025).
[107] Tianzi Luo, Xufeng Jing, Haiyong Gan, Chenxia Li, Zhi Hong, Laser Physics Letters **17**(12), 126203 (2020).
[108] M. A. Ahmed, D. Hu, Y. Shi, Y. Chen, S. Akhavan, Z. Yang, Photonic Sensors **15**, 250227 (2025).
[109] Y. Chen, X. Lei, X. Liu, P. Zhang, Photonic Sensors **15**, 250122 (2025).
[110] Xiaofeng Rao, Tao He, Chengfeng Li, Chao Feng, Zhanshan Wang, Yuzhi Shi, Xinbin Cheng, Acta Optica Sinica **2**(6), 0616001 (2025).
[111] F. Wang, H. Liu, T. Ma, M. Qian, Y. Liu, Photonic Sensors **15**, 250322 (2025).
[112] Jinfu Liu, Zhongzien Jiang, Xinhua Xu, Wenhao Li, Mengyuan Liu, Hong Liu, CAAI Transactions on Intelligence Technology **10**(6), 1646 (2025).
[113] Xubin Wu, Yan Niu, Xia Li, Jie Xiang, Yidi Li, CAAI Transactions on Intelligence Technology **10**(6), 1731 (2025).
[114] Y. K. Long, R. Min, K. Xiao, Z. Wang, L. Liu, Y. Sun, X. Li, Z. Li, Z. Zalevsky, Opto-Electronic Technology **1**, 250010 (2025).
[115] Guanjun Feng, Chen Wang, Yuming Lin, Mingfeng Zheng, Manna Gu, Fuhai Liu, Yong Tao, Yanling Li, Ying Tang, Ying Tian, J. Optoelectron. Adv. M. **27**(5-6), 219 (2025).
[116] C. Peng, J. Yao, D. P. Tsai, Opto-Electronic Technology **1**, 250004 (2025).

*Corresponding authors: today@zju.edu.cn
154495791@qq.com